Biomechan Model Mechanobiol (2005) 4: 168–177
DOI 10.1007/s10237-005-0073-z

ORIGINAL PAPER

M. R. Heistand · R. M. Pedrigi · S. L. Delange
J. Dziezyc · J. D. Humphrey

Multiaxial mechanical behavior of the porcine anterior lens capsule

Received: 14 January 2005 / Accepted: 8 April 2005 / Published online: 23 June 2005

Abstract The biomechanics of the lens capsule of the eye is important both in physiologic processes such as accommodation and clinical treatments such as cataract surgery. Although the lens capsule experiences multiaxial stresses in vivo, there have been no measurements of its multiaxial properties or possible regional heterogeneities. Rather all prior mechanical data have come from 1-D pressure–volume or uniaxial force-length tests. Here, we report a new experimental approach to study in situ the regional, multiaxial mechanical behavior of the lens capsule. Moreover, we report multiaxial data suggesting that the porcine anterior lens capsule exhibits a typical nonlinear pseudoelastic behavior over finite strains, that the in situ state is pre-stressed multiaxially, and that the meridional and circumferential directions are principal directions of strain, which is nearly equibiaxial at the pole but less so towards the equator. Such data are fundamental to much needed constitutive formulations.

Keywords Cataracts · Accommodation · Biomechanics · Stress · Stiffness

1 Introduction

The lens capsule is a thin, bag-like membrane that covers the lens of the eye; it consists primarily of type IV collagen (65% by dry weight) with admixed adhesion molecules and proteoglycans. The anterior lens capsule is approximately 60 μm thick in the porcine eye and 11–33 μm thick in the human eye (Krag et al. 1997a; Krag and Andreassen 2003). This capsule includes a monolayer of cuboidally shaped epithelial cells; these cells transform, near the equator, into the so-called equatorial bow cells (Fig. 1). The lens capsule maintains the lens in its proper position and acts as the means through which the ciliary muscles exert forces on the lens, changing its curvature during the process of accommodation.

In addition to its fundamental role in normalcy, the lens capsule plays a central role in clinical procedures such as cataract surgery. A cataract is a partial or total opacity of the lens that results in impaired vision or blindness. Over one-half of all Americans over age 65 develop a cataract, and cataract surgery has become the most frequently performed surgical procedure in the United States (~1.3 M/year). Briefly, in cataract surgery, the surgeon removes a portion of the anterior lens capsule, extracts the clouded lens, and replaces it with a prosthetic intraocular lens (IOL). Despite many advances in surgical technique and medical technology, the post-surgical complication of posterior capsule opacification (PCO) has occurred in up to 50% of all patients within 2–5 years following cataract surgery (Emery 1999; Spalton 1999). This PCO, or secondary cataract, results primarily from the epithelial cells migrating from the equatorial bow region of the lens capsule to the central region of the posterior lens capsule where they trans-differentiate, proliferate, synthesize matrix proteins (collagens I, III, etc.), cytokines and matrix metalloproteinases, and contract as in a wound healing response (Marcantonio and Vrensen 1999; Wormstone 2002; Saika et al. 2003). These symptoms of PCO often necessitate a second clinical intervention.

Fortuitously, a new intraocular lens design by Alcon Laboratories, Inc. (the AcrySof lens) has been reported to reduce PCO from the ~40–60% for other lenses to

M. R. Heistand · R. M. Pedrigi · S. L. Delange
J. D. Humphrey (✉)
Department of Biomedical Engineering, Texas A&M University,
337 Zachry Engineering Center 3120 TAMU,
College Station, 77843-3120, TX
E-mail: jhumphrey@tamu.edu
Tel.: +1-979-845-5558
Fax: +1-979-845-4450

J. Dziezyc
Department of Small Animal Medicine and Surgery,
College of Veterinary Medicine, Texas A&M University,
College Station, 77843-4474, TX

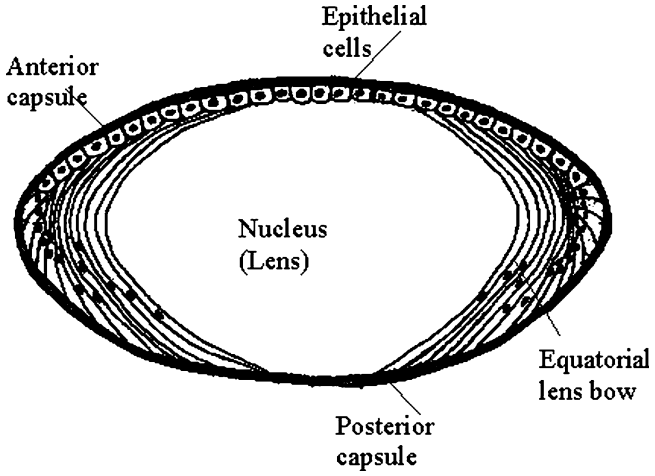

Fig. 1 Schematic drawing of the lens (including the nucleus and lens bow cells) and lens capsule (*outer covering*) illustrating the normal location of the epithelial cells and equatorial lens bow

~10% (Spalton 1999). Reports suggest that the two primary reasons for the marked improvement are the "sharp rectangular edge design" and possibly "increased adhesiveness" to the lens capsule (Linnola 1997; Nagata et al. 1998; Nishi et al. 2000). Indeed, because of the apparent mechanical advantages of the AcrySof lens, other mechanically motivated devices have been tried as well. For example, Nishi et al. (1997) increased the tension in the lens capsule, following cataract surgery, by implanting an inflatable endocapsular balloon. Alternatively, Nishi et al. (2001) reduced post-surgical shrinkage of the lens capsule by implanting a square-edged capsular bending ring. Both interventions reduced PCO, although not to the extent achieved with the AcrySof lens. Even though the pathophysiology of PCO remains uncertain, it is now clear that mechanical factors play a significant role, which emphasizes the need to quantify lens capsule mechanics.

Based on basic science and clinical observations reported in the literature, we hypothesize that perturbations from the native stress and strain fields within the lens capsule, due to cataract surgery, stimulate the errant response by the epithelial cells through mechanotransduction mechanisms. To test this hypothesis, we must first quantify the native stress and strain fields in the lens capsule and then compute or measure how these fields change due to various interventions and designs of intraocular implants. Toward this end, we must know the associated geometry, material properties, and applied loads. In this paper, we present the first experimental approach for investigating in situ the multiaxial mechanical behavior of the anterior lens capsule in enucleated eyes. Furthermore, we present the first detailed data on the regional, multiaxial, pseudoelastic behavior of the porcine anterior lens capsule. We submit that this is an important step towards understanding better both cataract surgery and mechanotransduction-induced PCO.

2 Methods

2.1 Experimental methods

Fresh porcine eyes were received following an overnight shipment in iced saline from SiouxPreme, Inc. (Idaho). The cornea and iris were excised, and the globe was secured in a moldable wax fixture using multiple pins placed through the peri-scleral tissue. Next, the exposed anterior lens capsule was allowed to air-dry at room temperature for 60 min so that 40-μm diameter fluorescent, polystyrene microspheres (Bangs Laboratories, Fishers, IN, USA) could be affixed to its surface to enable subsequent strain measurement. The hydrophobic nature of the microspheres results in a natural adhesion to type IV collagen, preventing their independent movement on the underlying lens capsule. These microspheres (or tracking markers) were arranged in multiple groups of five (one center marker and four corner markers), and these groups were then organized along the major and minor axes of the lens capsule, spanning from the anterior pole to the periphery near the equator (Fig. 2). The anterior pole was determined anatomically as the point on the lens capsule directly above the intersection of the Y-suture lines in the lens.

Next, a precision micro-manipulator was used to insert a 25-gauge needle just under the lens capsule (on the side opposite the markers). A cyanoacrylate adhesive was applied around the needle to seal the insertion site, and a physiologic saline solution was injected slowly into the lens. In most cases, the fluid flowed out of and then around the anterior portion of the lens, thus separating this portion of the lens capsule from the lens. Fig. 3 is an H&E stained cross-section of a lens capsule, shown in both a native and pressurized state; both were fixed via 24 h immersion in 10% formaldehyde, with the pressurized lens capsule perfusion-fixed at 30 mmHg. It is

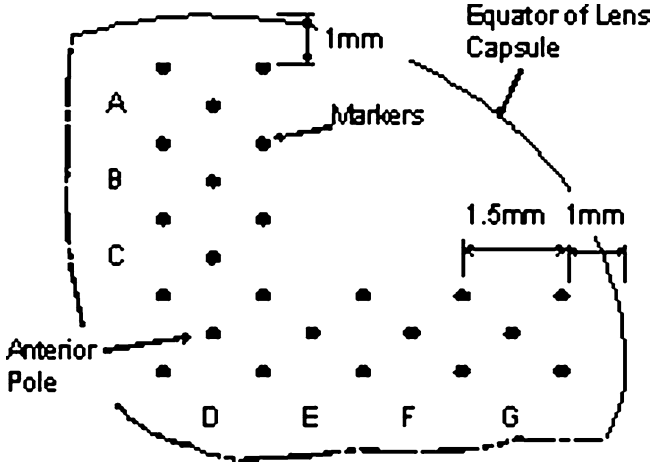

Fig. 2 Cut-away schematic view of the top right quadrant of an anterior lens capsule showing typical marker arrangements, consisting of seven overlapping sets of five markers (sets are denoted by *A–G*)

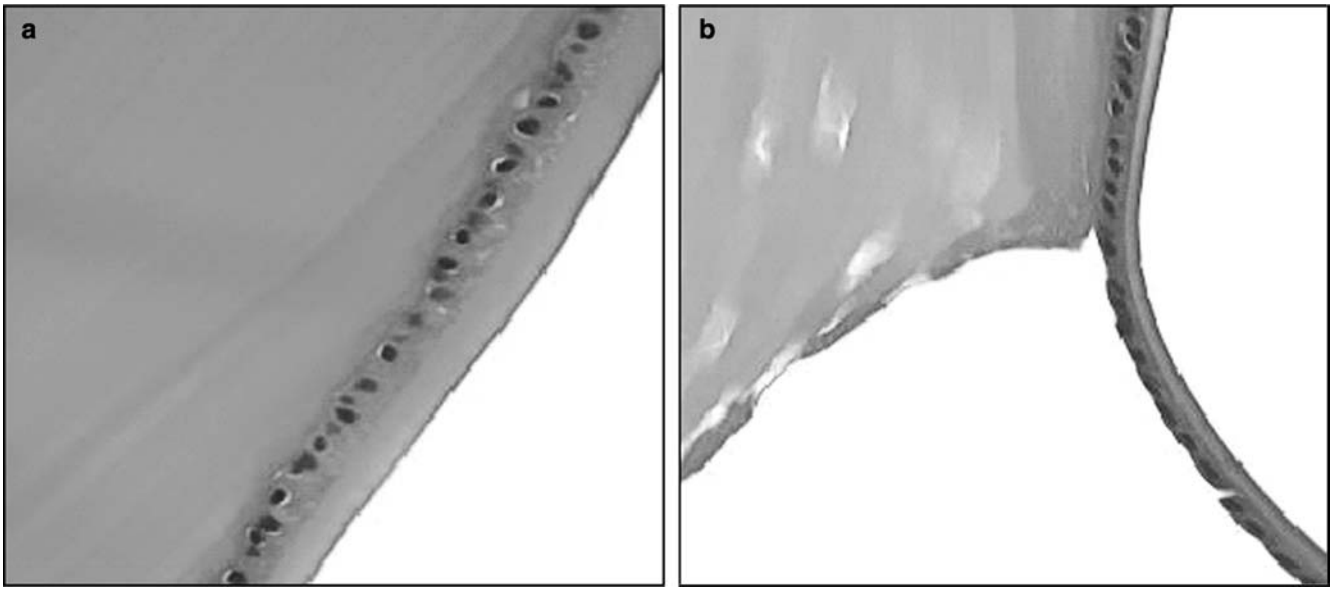

Fig. 3 Hematoxalin and eosin (H&E) stained histological cross-section of the porcine lens with lens capsule (40×). **a** Anterior lens capsule and lens in its native state. **b** Pressure distended (30 mmHg) anterior lens capsule. Note that the stretched epithelial cells remained on the anterior capsule, and there is a clean separation between these cells and the lens

evident from the figure that the epithelial cells remained on the fluid-separated anterior capsule.

Once the intact lens capsule was successfully separated from the underlying lens, the eye was immersed in a physiologic saline solution, warmed to 35°C (within 10 min), and rehydrated for 1 h (equivalent to the dehydration time). The specimen and specimen chamber were then positioned for testing so that the microspheres on the surface of the anterior lens capsule could be imaged at different distention pressures using the biplane video system described below.

2.2 Experimental System

Figure 4 shows the optical-mechanical components of a custom biplane, video-based test system. It includes: an optical table, a linear railway and carriage with a micro-adjustable translation stage and attached needle-injection micro-manipulator, a Plexiglas specimen chamber, a pressure transducer, a fluorescent light source, and two Sony CCD cameras, each outfitted with a long distance microscope lens (InfiniMax by Infinity Photo-Optical, Boulder, CO, USA). Not shown are the operating microscope (to the left of the optical table), two B&W monitors, a temperature controller, a video-multiplexer, a video cassette recorder, and a controller PC (with A/D and video frame-grabber boards). Note that the carriage-stage-needle-injection assembly can be translated as a rigid body along the railway, thus allowing the eye to be prepared under an operating microscope and then moved under the CCDs for mechanical testing while not disturbing the needle insertion within the eye.

The light source is a Jensen 150 W, high-intensity, white light illuminator. It illuminates the specimen via dual channel fiber optic light guides, coupled with focusable lenses. A shortpass filter having a sharp cutoff wavelength of 500 nm is mounted at the end of each light guide so the light source emits a deep blue color, ideal for exciting the fluorescent microspheres with excitation/emission maxima of 480/520 nm. Broadband filters (CWL: 520 nm, FWHM: 40 nm) are mounted in front of each camera to filter out background light as well as reflected light from the light source.

The cameras are arranged so that one is directly above the specimen, with its visual axis perpendicular to the optical table, while the other is oriented 45° from the

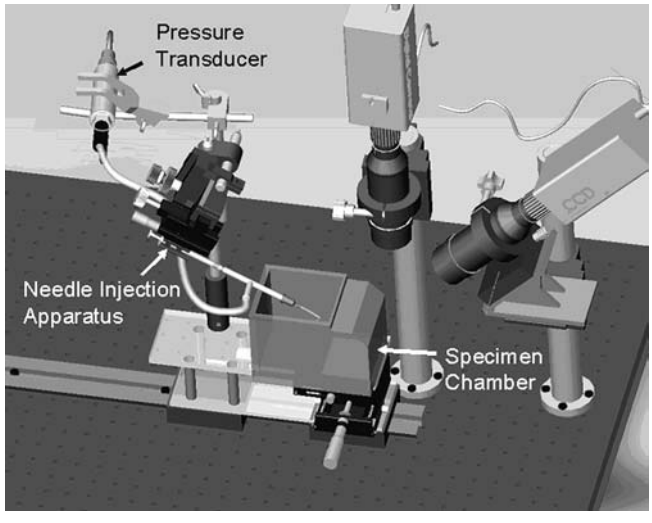

Fig. 4 Computer drawing of the primary components of the experimental system, namely a temperature-controlled specimen chamber, an inflation system consisting of a needle, micromanipulator, and pressure transducer, and finally, a bi-plane video system

first so their visual axes intersect at 45° in a plane that is perpendicular to the optical table. The angled camera is mounted to a vertical translational stage so that the intersection of the visual axes can be moved up and down to match the specimen's height, allowing both cameras to image the same section simultaneously. Furthermore, each camera is mounted to an additional translation stage to allow precise movement along its visual axis, thus providing independent adjustment of focus for each camera.

2.3 3D Marker Reconstruction

Global reconstruction techniques can be used with the biplane video system to rebuild three-dimensional objects from two separate, two-dimensional images. The process is simplified in our case since we are imaging microspheres and mapping the camera coordinates of their centroids into point space. Therefore, our system must determine the location of an arbitrary point in a three-dimensional Euclidean space, given two separate camera views of a marker with its centroid located at that point. This can be described mathematically as finding the 3D coordinates of a point defined via a position vector **p** with respect to two orthogonal coordinate systems given by unit vectors [**e**, **f**, **g**] and [**e***, **f***, **g***], where the projection tensors $\mathbf{P}_1 = \mathbf{I} - \mathbf{g} \otimes \mathbf{g}$ and $\mathbf{P}_2 = \mathbf{I} - \mathbf{g}* \otimes \mathbf{g}*$ operate on **p** to give the perpendicular projections onto the viewing planes of the two cameras (Fig. 5).

We assume a linear relationship between image coordinates and the spatial location **p** (centroid of a marker), so that determination of 3D coordinates for a given point requires calculation of the twelve constants in the transformation equation

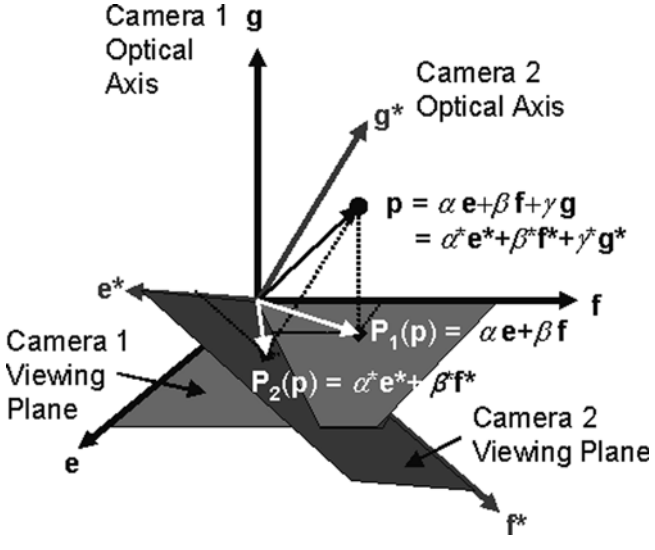

Fig. 5 A point viewed by each camera is located by the perpendicular projection of its position vector onto a plane orthogonal to the optical axis of each camera

$$N_i^{(j)} = A_{ik}^{(j)} X_k^{(j)}, \quad (k \text{ sum 1 to 3}),$$

where N_i is the coordinate of a point for each camera in pixels, with $j = 1,2$ indicating the camera and $i = 1,2$ indicating the 2D directions. The twelve calibration constants are given by $A_{ik}^{(j)}$, and the 3D Cartesian coordinates are given by $X_1^{(j)}, X_2^{(j)}, X_3^{(j)}$ with respect to the orthogonal basis vectors [**e**,**f**,**g**] for $j = 1$ and [**e***, **f***, **g***] for $j = 2$ (see Fig. 5).

The camera lenses provide constant magnification through their depth of view, thus N_i does not depend on X_3. Furthermore, there are no appreciable visual distortions in the field of view so that N_1 does not depend on X_2 and N_2 does not depend on X_1; this reduces the number of calibration constants from twelve to four. Our video system is also orientated so that one camera view is known relative to the second (in Fig. 5, **e** = **e*** and **g*** is rotated θ = 45° clockwise from **g**), thus $X_k^{(1)}$ and $X_k^{(2)}$ are related by the coordinate transformation matrix

$$\begin{bmatrix} X_1^{(2)} \\ X_2^{(2)} \\ X_3^{(2)} \end{bmatrix}_{e^*, f^*, g^*} = \begin{bmatrix} 1 & 0 & 0 \\ 0 & \cos\theta & -\sin\theta \\ 0 & \sin\theta & \cos\theta \end{bmatrix} \begin{bmatrix} X_1^{(1)} \\ X_2^{(1)} \\ X_3^{(1)} \end{bmatrix}_{e, f, g}.$$

The four calibration constants (rewritten as B_i for $i = 1$ to 4) can be found with respect to a single set of basis vectors by individually solving the decoupled equations

$$N_1^{(1)} = B_1 X_1 \qquad N_1^{(2)} = B_3 X_1$$
$$N_2^{(1)} = B_2 X_2 \qquad N_2^{(2)} = B_4 (X_2 \cos\theta - X_3 \sin\theta),$$

for known camera coordinates N_i of imaged points with known spatial coordinates X_k, where the 3D Cartesian coordinates given by X_k are taken with respect to the orthogonal basis vectors [**e**,**f**,**g**]. Once these constants are found, they can be used in the same equations to solve for the 3D coordinates of each marker, given camera coordinates of its centroid from both cameras.

The camera coordinates of each marker centroid were calculated from digitized images using a custom code developed with National Instruments IMAQ Vision software. The coordinates for each centroid were returned in pixel values, indicating their respective location in the pixel domain of the 640 by 480 digitized image.

Additionally, we are interested in finding the 3D coordinates of all marker centroids relative to each other. That is, we must calculate the 3D global coordinates of each centroid with respect to some arbitrary laboratory origin, but the field of view for each camera is not wide enough to capture all the markers simultaneously. Therefore, several overlapping images were taken such that subsequent images involved a calculated translation of the stage and contained at least one marker visible in the previous image. The images were then stitched together to form a montage so that coordinates for each marker were with respect to a common

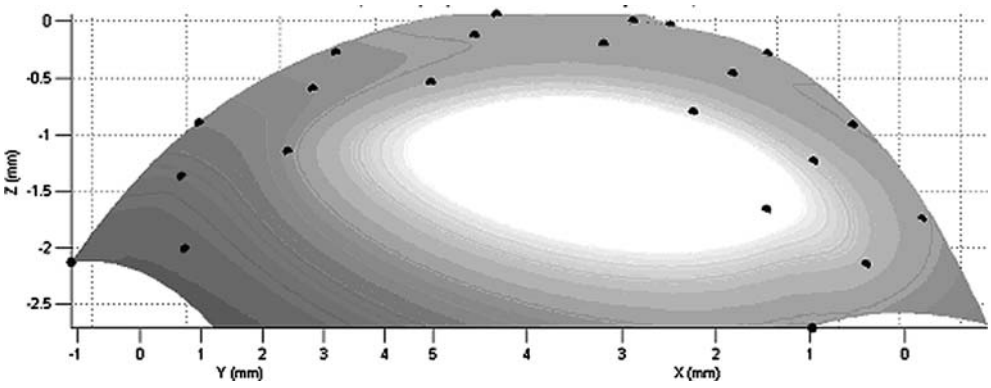

Fig. 6 Plot of global 3D coordinates of markers on the anterior surface of a pressurized lens capsule (the surface shown is fitted to marker coordinates using biharmonic spline interpolation functions; this surface, with computer-generated lighting effects, is displayed for visualization purposes only)

point. The 3D reconstruction method discussed above could then be used to calculate the global 3D Cartesian coordinates of all markers; this yielded coordinates in millimeters, with respect to an origin chosen at the anterior pole (see Fig. 6).

The resolution of the experimental system depends on that of the individual components. The pressure transducer is accurate to within $\pm 0.1\%$ full scale; current resolution is 0.05 mmHg. The image resolution for each camera is 130 pixels/mm, and the high-contrast images of fluorescent microspheres, coupled with the enhanced image filtering capabilities of the National Instruments IMAQ Vision software, allows us to measure distances between marker centroids, approximately 2 mm apart, to within less than a half pixel error. Considering all sources of error, our biplane video system still provides a measure of strain within 1% error.

2.4 Experimental Protocols

The lens capsule was pressurized slowly by raising a fluid reservoir via a pulley system. The reservoir contained saline solution and was connected to the pressure transducer and inserted needle, thus allowing control of the distension pressure. The lens capsule was inflated in increments of 5 mmHg, with 2 min at each pressure state, so as to cycle the pressure from 0 mmHg to 45 mmHg to 0 mmHg five times. In one series of studies, marker positions were determined at each pressure state during the first and fifth loading and unloading cycles. In another series, the lens capsule was inflated incrementally through only one cycle, and a creep test was performed thereafter at 45 mmHg. In other words, the pressure was raised suddenly from 0 mmHg to 45 mmHg in the lens capsule (within ~5 s), and then maintained constant. The final aspect of the experimental procedure involved obtaining a nearly stress-free configuration. This was accomplished by isolating the lens capsule and lens from the eye and then cutting the posterior lens capsule away to allow free movement of the anterior capsule. The markers were then imaged as the anterior lens capsule rested freely on the lens.

2.5 Calculation of strain

Monitoring the 3D motions of markers on the surface of the inflating lens capsule permits one to calculate the associated displacement gradients, and in turn, regional in-plane Green strains of the capsule. The specific arrangement of markers in sets of five allows one to construct four triangles of similar size and shape in each set (see Fig. 7), where the corners of each triangle constitute a triplet of markers. A triplet of markers is the minimum set needed for calculating all three in-plane components of strain (Humphrey 2002).

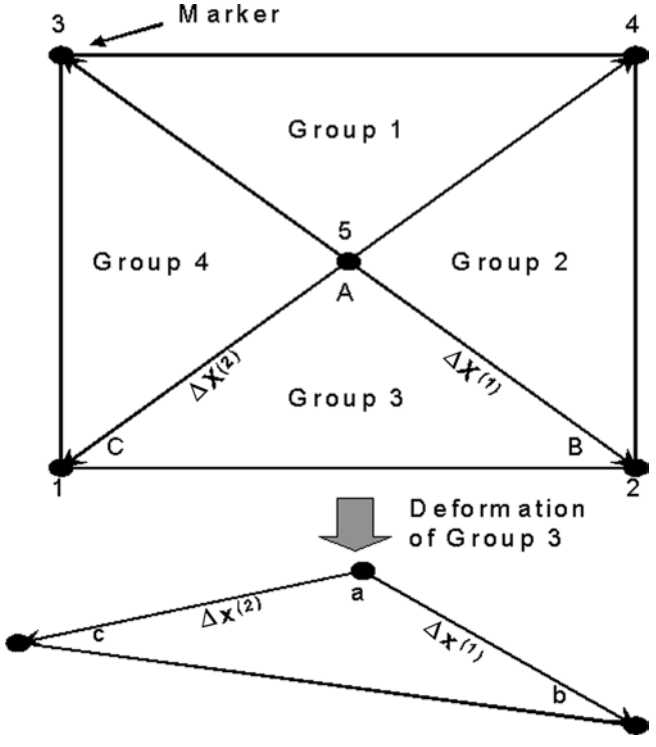

Fig. 7 Standardized subdivision of each marker set into four groups of marker triplets for strain calculation. Position vectors can be constructed from a triplet of markers, as illustrated, for the purpose of calculating the deformation gradient

Finite Green strains, **E**, were computed locally for each triplet using the deformation gradient, **F**, through the equation $\mathbf{E}=(\mathbf{F}^{\mathrm{T}}\ \mathbf{F}-\mathbf{I})/2$. The three components of in-plane strain for each marker triplet are labeled as meridional, circumferential, and shear; the origin of the localized strain region was prescribed to coincide with the centroid of the triplet. The meridional component of strain always points to the anterior pole of the lens capsule and is tangent to the capsule at the triplet centroid. In addition, the circumferential direction is tangent to the lens capsule at the centroid of the triplet and is perpendicular to the meridional direction, as illustrated in Fig. 8.

The deformation gradient can be calculated directly for each marker triplet by finding how position vectors ($\Delta X^{(1)}=X_{\mathrm{B}}-X_{\mathrm{A}}$ and $\Delta X^{(2)}=X_{\mathrm{C}}-X_{\mathrm{A}}$) in a reference configuration deform to position vectors ($\Delta x^{(1)}=x_{\mathrm{b}}-x_{\mathrm{a}}$ and $\Delta x^{(2)}=x_{\mathrm{c}}-x_{\mathrm{a}}$) in subsequent configurations representing various distension pressure states (e.g., Fig. 7). Because the marker triplets are close together, we assumed a homogeneous deformation within each triangular region created by a marker triplet. Thus, $\Delta\mathbf{x}\approx\mathbf{F}(\Delta\mathbf{X})$ and the in-plane components of **F** can be determined for each pressure state using the matrix equation

$$\begin{bmatrix}\Delta x_1^{(1)} & \Delta x_1^{(2)}\\ \Delta x_2^{(1)} & \Delta x_2^{(2)}\end{bmatrix}=\begin{bmatrix}F_{11} & F_{12}\\ F_{21} & F_{22}\end{bmatrix}\begin{bmatrix}\Delta x_1^{(1)} & \Delta x_1^{(2)}\\ \Delta x_2^{(1)} & \Delta x_2^{(2)}\end{bmatrix}.$$

Note the standardized calculation of position vectors illustrated in Fig. 7 for each marker set, where all position vectors originate at the center marker of the set.

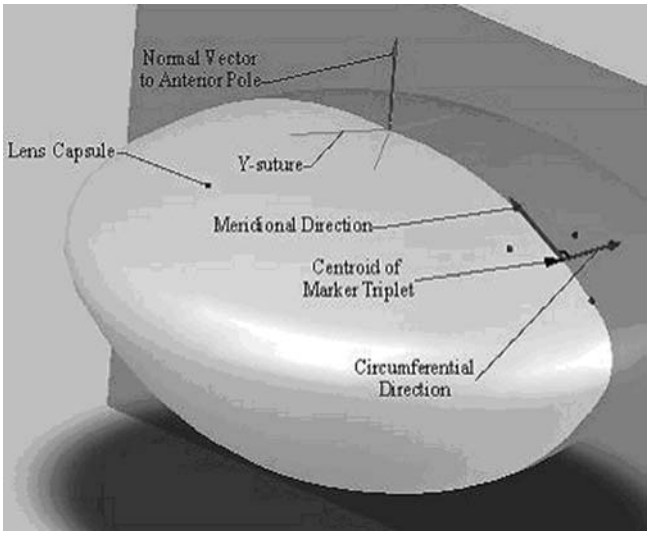

Fig. 8 Schema of the lens capsule showing the directions for the different components of strain, which originate at the centroid of each marker triplet

3 Results

Figure 9 shows the typical strain response of the lens capsule for loading and unloading during the first and fifth cycle, with respect to the in-situ, unloaded reference configuration. Note the slight increase in strain magnitude of the fifth cycle over the first cycle and the slight hysteresis; both suggest a preconditioning effect (cf. Fung 1990). Figures 10 and 11 show pressure–strain data at the anterior pole (Set D) and near the equator

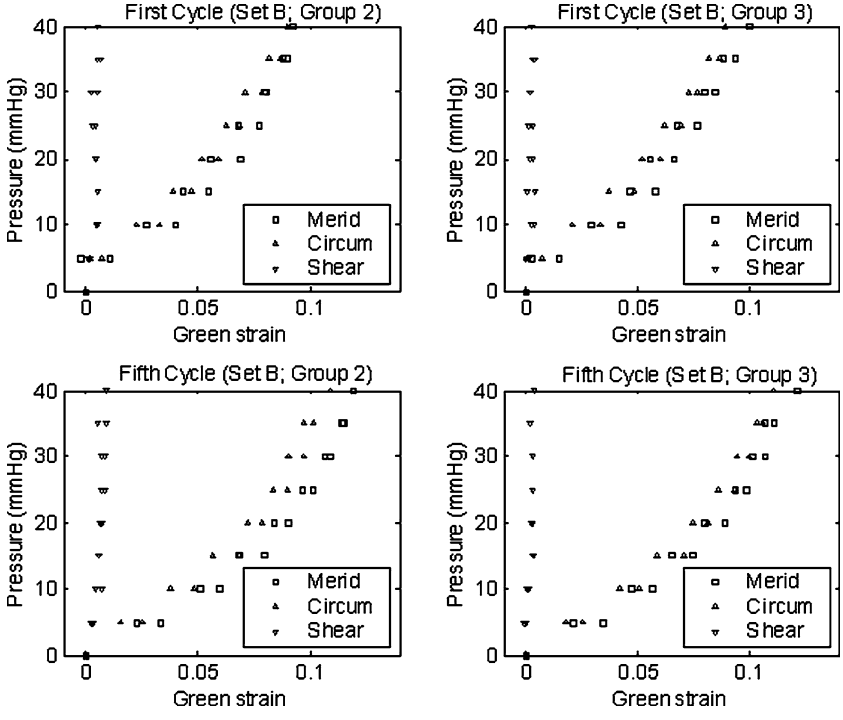

Fig. 9 Comparison of meridional, circumferential, and shear components of strain for the first and fifth cycle of pressurization to 40 mmHg, with respect to the in-situ unloaded reference configuration (see Figs. 2 and 7 for the location of each marker triplet)

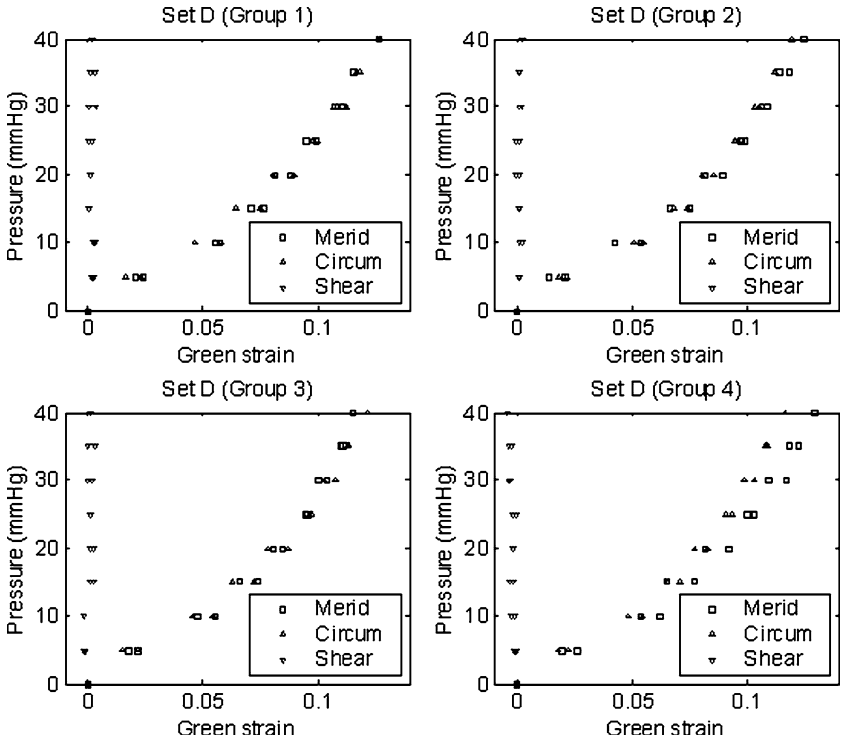

Fig. 10 Plot of all components of strain for marker set D during the fifth cycle, with respect to the in-situ unloaded reference configuration. Note the consistency amongst the four sets of data within the region, thus supporting the computational assumption of local homogeneity over regions less than 2×2 mm. Furthermore, the near equibiaxial strains suggest a symmetry about the apex of the capsule

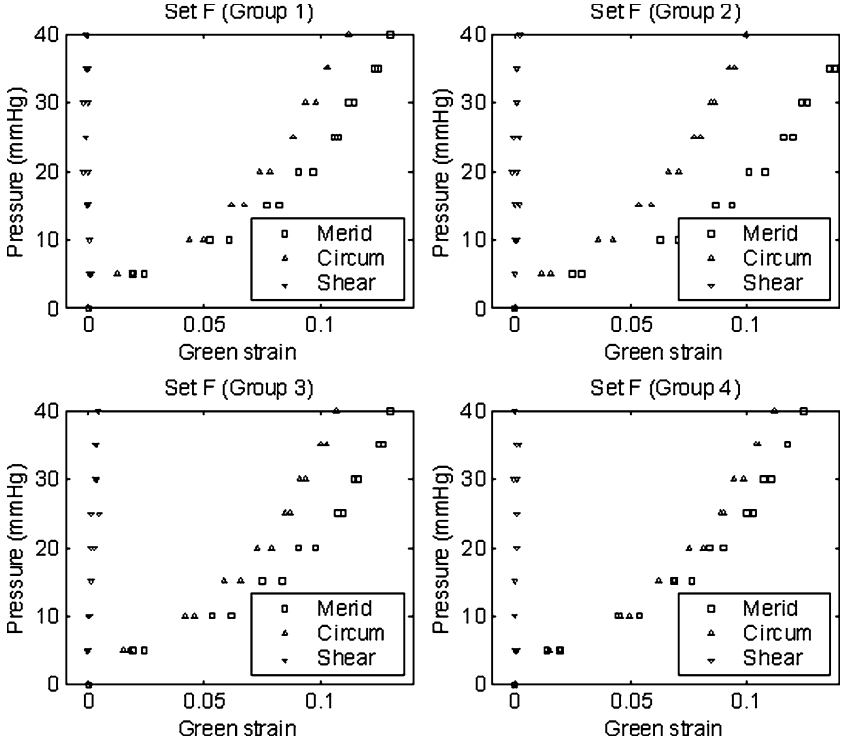

Fig. 11 Plot of all components of strain for marker set F during fifth cycle, with respect to the in-situ unloaded reference configuration. Note that the strains are greater in the meridional than in the circumferential direction. This is consistent with a circumferential constraint at the equator. Indeed, note that the directional difference is greatest in group 2, as expected, which is closest to the equator

(Set F) for all four marker triplets during the fifth cycle. The responses are nonlinear in the meridional and circumferential directions and approximately zero for shear in all four groups of both marker sets. This is an important observation for it reveals that the meridional and circumferential directions are principal directions. The meridional component of strain also appears to be greater than the circumferential component near the equator, but approximately the same at the anterior pole. The components of strain at 40 mmHg, with re-

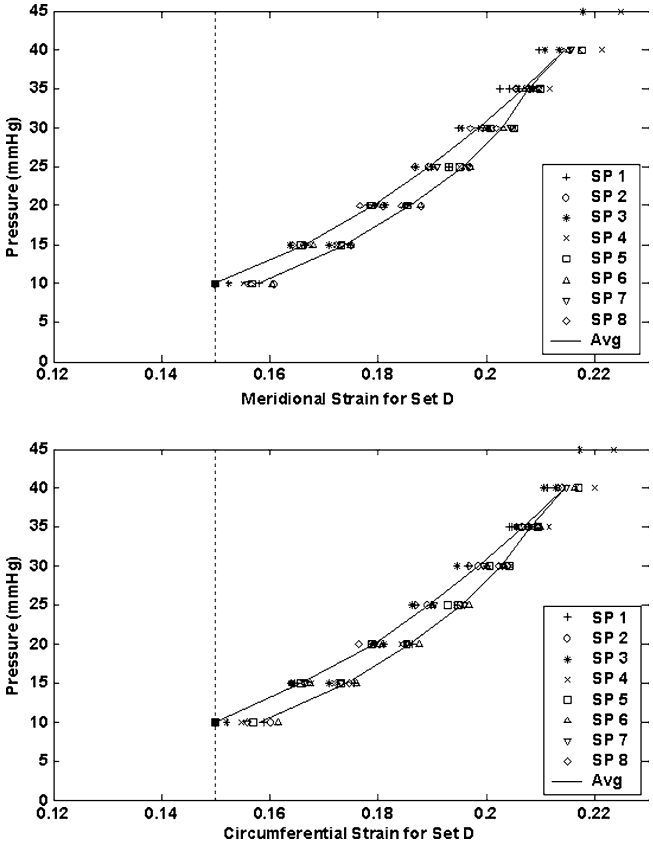

Fig. 12 Plot of loading and unloading curves from Set D of eight experiments, where the strain is measured using the pressure state at 10 mmHg as the reference, and the initial strain (strain at 10 mmHg with respect to the stress-free configuration) is assumed to be roughly 15%, which is the average initial strain calculated from five experiments. Note the consistency of the data, demonstrating the repeatability of our experimental method

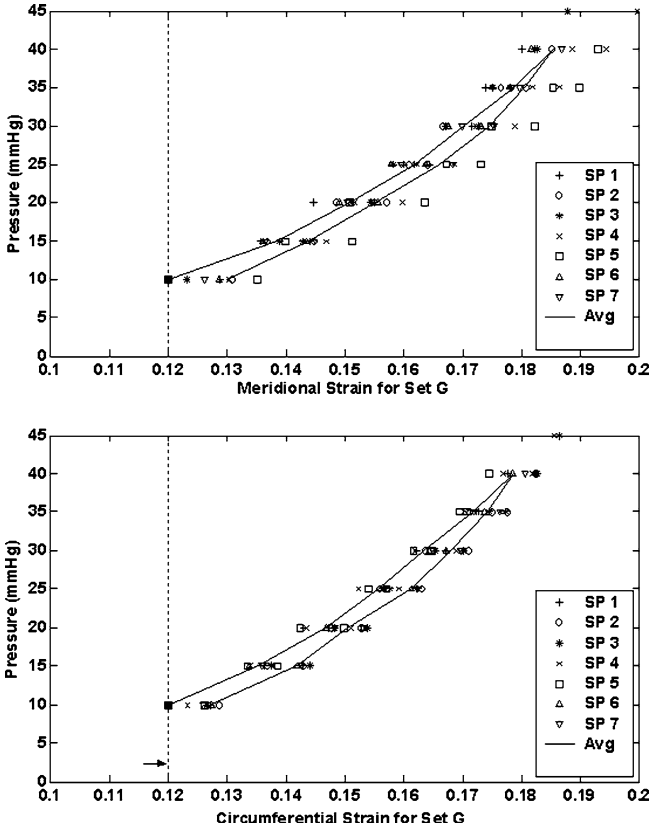

Fig. 13 Plot of loading and unloading curves from Set G of seven experiments, where the strain is measured using the pressure state at 10 mmHg as the reference, and the initial strain (strain at 10 mmHg with respect to the stress-free configuration) is assumed to be roughly 12%, which is the average initial strain calculated from two experiments

spect to the in-situ, unloaded state, were typically around 10%–12%.

The strains in the meridional and circumferential directions from Set D and Set G, for eight specimens, are shown in Figs. 12 and 13, respectively; the solid line indicates the mean loading and unloading data for all specimens pressurized to 40 mmHg. The 10 mmHg pressure state is used as the reference for measuring strain due to possible interactions between the lens and lens capsule that created difficulties in obtaining pressure states below 10 mmHg for some of the experiments. Nevertheless, separate information from the stress-free, reference configuration provides an estimate of strain at 10 mmHg. Figure 14 shows the strain from the stress-free reference for the different regions from five separate experiments. Note that the average strain at 10 mmHg was used to horizontally shift the strain curves in Figs. 12 and 13. Therefore, the strain at 40 mmHg with respect to the stress-free, reference configuration was roughly 20% (biaxially), owing to a pre-strain (strain in the in-situ, unloaded state compared to the stress-free state) of roughly 12–15% in both the meridional and circumferential directions.

Figure 15 shows creep data from a representative specimen. It is important to note that this static system could measure, at best, the strains 1 min after the distension pressure (45 mmHg) was applied; correspondingly, any early creep response was not measured. It should be noted, however, that creep is primarily a long-term response, and very little creep was observed over the 30 min period.

4 Discussion

Despite its fundamental importance in physiologic processes such as accommodation and clinical interventions such as cataract surgery, our understanding of the mechanical behavior of the lens capsule remains incomplete. Early work by Fisher (1969) suggested that the ultimate tensile stress of the human anterior lens capsule decreases with aging from 2.3 MPa to 0.7 MPa, yet these results are limited by both the experimental set-up and the method of data analysis. Data were collected via pressure–volume tests, which are essentially 1-D and averaged over multiple regions and directions, and data

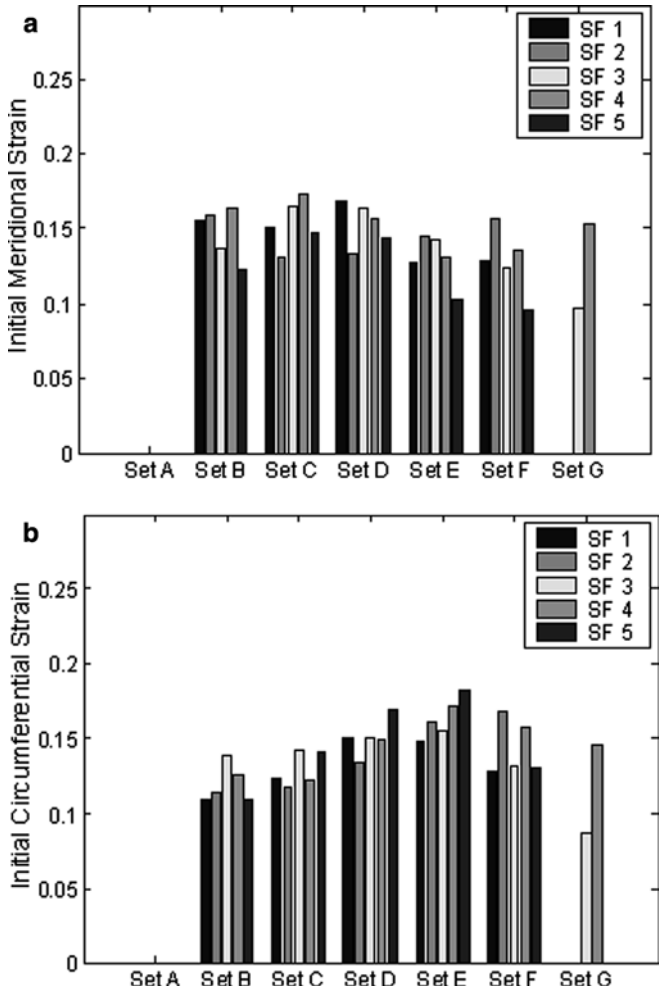

Fig. 14 Measured initial strains (strains at 10 mmHg with respect to the stress-free configuration) by region. Note that markers are often lost near the equator when cutting the anterior lens capsule free for this measurement

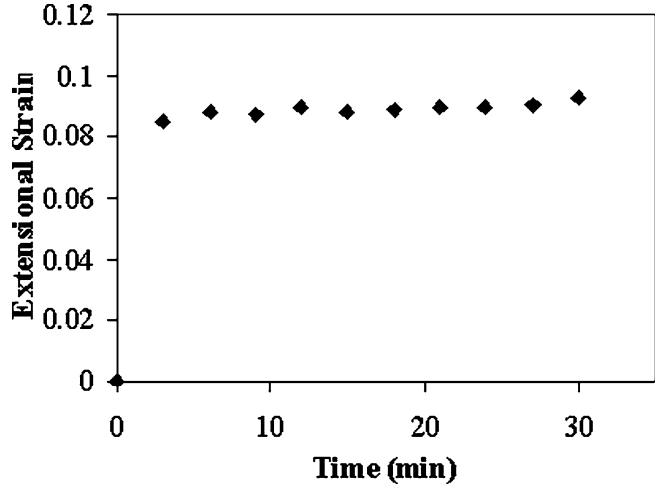

Fig. 15 Mean creep response at a constant pressure (45 mmHg) relative to the in-situ, unloaded configuration from Set F

were reduced using a result from linearized elasticity. The latter is inappropriate given the nonlinear material behavior and finite strains.

There are also data from various "unconventional" mechanical tests. For example, Krag et al. (1993) measured the pressure required to express the lens following a continuous circular capsulorhexis (CCC). They found that the posterior lens capsule ruptures at 59 ± 10 mmHg, whereas effective "hydroexpression of the lens" required pressures from 3 mmHg to 47 mmHg (lower pressures for larger CCCs). Yang et al. (1998) measured the force required for a 0.455-mm diameter rod to puncture the lens capsule when applied normal to the surface. They found that the force required for penetration was significantly higher in the anterior than in the posterior (9.02 g versus 4.42 g) lens capsule.

Most recently, many important findings on the uniaxial mechanical and thermomechanical behavior of the porcine and human lens capsule were reported by Krag and Andreassen (2003) and Krag et al. (1996, 1997b, 1998). Briefly, they tested intact, circumferential rings of lens capsule in uniaxial tension. Data revealed a highly nonlinear stress–strain relation, with stresses on the order of 4–5 MPa at stretches of 60%–80% (1st Piola-Kirchhoff stress vs. linearized strain), with no statistically significant difference in behavior between the left and right eye from the same donor. Moreover, despite marked differences in thickness, they found the stress–strain behavior to be the same for the anterior and the posterior capsule. Finally, it was found that mechanical strength and distensibility decrease with age while thickness and stiffness increase with age. These are important findings. Bailey et al. (1993) similarly reported uniaxial stress-strain data, although as a function of the degree of glycation cross-linking due to incubating porcine lens capsules in a 133-mM glucose solution. As expected, the data reveal that the lens capsule becomes stiffer and less extensible with increasing cross-links, which likely reflects that which occurs in diabetes and aging.

Uniaxial data provide important insight into some characteristics of the behavior of a material, but they are not sufficient for delineating the multiaxial behavior that exists in vivo. There is, therefore, a pressing need for multiaxial data. Moreover, it is often preferable to test biological tissues while maintaining their native geometry and mimicking native loading conditions. This is often complicated by the presence of adherent tissue, however, which is why many tissues are excised for testing. We developed a new technique whereby the lens capsule can be isolated from the underlying lens, loaded by a pressure that induces in-plane stresses, and yet maintained in nearly their native geometry, with natural boundary conditions around the periphery. Consistent with uniaxial findings, we observed a nonlinear material behavior over finite strains. In addition, we found very little creep in the anterior capsule over 30 min when subjected to a 45-mmHg pressure. Finally, we found that the strain in the lens capsule varies with region and

direction. The meridional strain always appeared to be equal to or greater than the circumferential strain, their difference being most notable near the equator. These results are not unexpected; indeed, they are qualitatively similar to results obtained for other nonlinear biological membranes such as intracranial saccular aneurysms (Humphrey 2002).

We emphasize that this experiment focuses on the quantification of mechanical properties, not on the study of a particular in vivo situation. Because of the inherent geometric and material complexities, analysis of in vivo conditions will require finite element or comparable numerical studies.

In conclusion, we recall that there are five primary steps to formulate a constitutive relation: delineate general characteristic behaviors, establish an appropriate theoretical framework, identify the specific functional form, calculate the values of the material parameters, and evaluate the predictive capability (Humphrey 2002). Based on the present findings, it appears that a nonlinear pseudoelastic membrane theory may be useful to quantify the material behavior of the anterior lens capsule with the possible need to account for anisotropy or regional heterogeneity. Now that we have a novel method to collect the requisite multiaxial data, there is a need to formulate a constitutive descriptor appropriate for nonlinear finite element analysis.

Acknowledgments This research was supported, in part, by grants from the Texas Advanced Technology Program (000512-0097-2001; 000512-0013-2003) and by a contract from Alcon Laboratories, Inc., Fort Worth Texas. In particular, we wish to thank Drs. M. Karakelle and K. Chan at Alcon for encouragement and support throughout this project and J.-J. Hu for help with the histology.

References

Bailey AJ, Sims TJ, Avery NC, Miles CA (1993) Chemistry of collagen cross-links: Glucose-mediated covalent cross-linking of type-IV collagen in lens capsules. Biochem J 296:489–496

Emery J (1999) Capsular opacification after cataract surgery. Curr Opin Opthalmol 10:73–80

Fisher RF (1969) The significance of the shape of the lens and capsular energy changes in accommodation. J Physiol 201:21–47

Fung YC (1990) Biomechanics: mechanical properties of living tissue. Springer, Berlin Heidelberg New York

Humphrey JD (2002) Cardiovascular solid mechanics: cells, tissues, and organs. Springer, Berlin Heidelberg New York

Krag S, Andreassen TT (1996) Biomechanical measurements of the porcine lens capsule. Exp Eye Res 62:253–260

Krag S, Andreassen TT (1998) Effect of freezing on lens capsule mechanical behavior. Ophthalmic Res 30:280–285

Krag S, Andreassen TT (2003) Mechanical properties of the human lens capsule. Prog Retin Eye Res 22:749–767

Krag S, Thim K, Corydon L (1993) Strength of the lens capsule during hydroexpression of the nucleus. J Cat Refract Surg 19:205–208

Krag S, Olsen T, Andreassen TT (1997a) Biomechanical characteristics of the human anterior lens capsule in relation to age. Invest Ophthalmol Vis Sci 38:357–363

Krag S, Danielsen CC, Andreassen TT (1997b) Thermal and mechanical stability of the lens capsule. Curr Eye Res 17:470–477

Linnola RJ (1997) Sandwich theory: Bioactivity-based explanation for posterior capsule opacification. J Cat Refract Surg 23(10):1539–1542

Marcantonio J, Vrensen GFJM (1999) Cell biology of posterior capsulater opacification. Eye 13:484–488

Nagata T, Minakata A, Watanabe I (1998) Adhesiveness of acrysof to a collagen film. J Cat Refract Surg 24:367–370

Nishi O, Nakai Y, Mizumoto Y, Yamada Y (1997) Capsule opacification after refilling the capsule with an inflatable endocapsular balloon. J Cat Refract Surg 23:1548–1555

Nishi O, Nishi K, Wickstrom K (2000) Preventing lens epithelial cell migration using intraocular lenses with sharp rectangular edges. J Cat Refract Surg 26:1543–1549

Nishi O, Nishi K, Menapace R, Akura J (2001) Capsular bending ring to prevent posterior capsule opacification: 2 year follow-up. J Cat Refract Surg 27:1359–1365

Saika S, Miyamoto T, Ishida I, Obnishi Y, Ooshima A (2003) Osteopontin: A component of matrix in capsular opacification and subcapsular cataract. IOVS 44:1622–1628

Spalton DJ (1999) Posterior capsular opacification after cataract surgery. Eye 13:489–492

Wormstone IM (2002) Posterior capsule opacification: A cell biological perspective. Exp Eye Res 74:337–347

Yang X, Zou L, Binrong M, Dong D, Dai H, Lu X (1998) Tensile strength of lens capules in eye-bank eyes. J Cat Refract Surg 24:543–546